IEEE Access
Multidisciplinary ⋮ Rapid Review ⋮ Open Access Journal

Received 3 September 2024, accepted 3 November 2024, date of publication 7 November 2024,
date of current version 19 November 2024.

Digital Object Identifier 10.1109/ACCESS.2024.3493601

RESEARCH ARTICLE

Assessment of 3D Integral Imaging Information Loss in Degraded Environments

PRANAV WANI, KASHIF USMANI, GOKUL KRISHNAN, AND BAHRAM JAVIDI, (Fellow, IEEE)
Electrical and Computer Engineering Department, University of Connecticut, Storrs, CT 06269, USA

Corresponding author: Bahram Javidi (Bahram.javidi@uconn.edu)

The work of Bahram Javidi was supported in part by the Air Force Office of Scientific Research under Grant FA9550-21-1-0333, Grant FA9550-24-1-0128; in part by Office of Naval Research under Grant N000142212375 and Grant N000142212349; and in part by the National Science Foundation under Grant 2141473.

ABSTRACT This paper presents an experimental analysis of information loss in degraded environments for traditional 2D imaging and 3D integral imaging. We consider mutual information to quantify this information loss. Our experimental analysis shows that 3D integral imaging preserves more scene information in degraded environments considered here than traditional 2D imaging. Additionally, as an example of the effects of information loss, we experimentally analyze the performance of integral imaging-based object depth localization in foggy environments. We compare the performance of three commonly used integral imaging based depth localization methods, that is, mutual information, minimum variance, and maximum voting strategy in foggy environments. For this purpose, we use illustrative laboratory scenes recorded in varying fog levels with and without partial occlusions. We assume the availability of bounding boxes corresponding to each object. An increase in fog severity results in increased information loss as measured by mutual information. Our analysis shows that all three algorithms perform comparably in clear environments and can localize an object's depth with good accuracy. The depth localization accuracy decreases in light to moderate foggy environments. However, mutual information provides more accurate depth information for light to moderate foggy environments compared to the other two methods. All three algorithms fail to provide reliable depth information for severe foggy environments.

INDEX TERMS Depth estimation, fog, integral imaging, low light illumination, maximum voting strategy, minimum variance, mutual information, partial occlusion.

I. INTRODUCTION

Integral imaging is a prominent multi-camera imaging technique that records angular information about the incoming light field [1], [2], [3], [4], [5]. Traditional integral imaging used a lenslet array in front of a single imaging sensor. However, this technique has a limited parallax. The parallax can be further increased by using a synthetic aperture integral imaging setup [6], [7], [8], [9], [10], [11], [12], [13], [14], [15], [16]. It captures multiple 2D elemental images of a scene from different perspectives. We use a single camera mounted on a translation stage to record multiple 2D elemental images. However, the same can be achieved by using a camera array. One of the several applications of InIm is in passive depth localization [17], [18], [19], [20], [21] which has been further advanced to account for partial occlusions [22], [23], [24], [25], [26]. InIm has proven useful for imaging in several adverse environmental conditions such as low illumination and fog [27], [28].

Mutual information (MI) is a statistical measure of the non-linear similarity between two data sources. Shannon's research is largely credited for the development of mutual information [29]. Since then, mutual information has been used in several fields, including communication theory, statistics, and complexity analysis [30]. Registration of multi-modal medical images like MR and CAT images is an application of mutual information [31], [32] in image analysis. Here mutual information was used as a measure of pixel correspondence between two different images of the same body part. Several studies subsequently showed that mutual information performed at a similar level compared to manual-assisted registration [33]. Recently, mutual information has been used for a wide range of applications such as a stereo correspondence measure [34], image

The associate editor coordinating the review of this manuscript and approving it for publication was Derek Abbott.

registration [35], [36], and as an image similarity metric [37], [38]. Mutual information has also been utilized for image fusion [39], and multi-plane tracking [40]. We utilize mutual information as a metric to quantify the information present in a scene in the presence of degraded environments like fog, partial occlusion, and low illumination conditions.

This manuscript presents mutual information-based information loss analysis between 3D integral imaging and 2D imaging under varying degradations. Our experimental analysis shows that 3D integral imaging can better preserve the scene information in degraded environments than traditional 2D imaging. Additionally, as an illustrative example of the effects of information loss in degraded environments, we experimentally analyze integral imaging based object depth localization performance in foggy environments. We compare three integral imaging-based depth localization methods for two illustrative laboratory scenes recorded in varying levels of fog. These methods are minimum variance [41], maximum voting [18], and mutual information [42], [43]. The information regarding spatial location (bounding box) is assumed to be available for each object. We can use approaches such as deep learning-based object detection for such information characterization. Our analysis shows that all three object depth localization algorithms perform comparably in clear environments. However, for light to moderate foggy environments, the mutual information-based approach provides much more accurate object depth information compared to the other two methods. For severe foggy environments, all three algorithms fail to provide reliable depth information. Still, for severely foggy environments, the mutual information based approach provides comparatively more accurate object-depth information than other methods.

II. 3D INTEGRAL IMAGING

Integral imaging uses diverse perspectives of incoming light fields to achieve passive 3D imaging of the scene. We use a single camera mounted on a translation stage to capture elemental images. However, the same can be achieved with either a lenslet array in front of a single imaging sensor or by using a camera array [6], [7], [8], [9], [10], [11], [12], [13], [14], [15], [16]. Captured 2D elemental images can be back-propagated through a virtual pinhole to obtain a faithful 3D reconstruction of the original scene. This technique is optimal in the maximal likelihood sense for images dominated by Gaussian noise, which usually happens in low illumination conditions where read noise dominates the image capture process [2], [3], [4], [5]. This results in the 3D reconstructed scene having a better signal-to-noise ratio compared with any individual 2D elemental images in low illumination conditions. More information and a review of integral imaging and its applications can be found in [44] and [45].

In our experiments, we use a synthetic aperture integral imaging setup which has a higher parallax compared to the traditional integral imaging setup which uses a lenslet array in front of a single imaging sensor [46]. Figure 1(a) shows

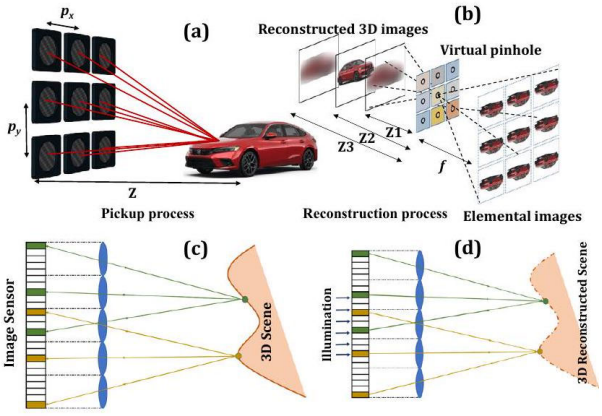

FIGURE 1. (a) Synthetic aperture integral imaging (InIm) setup using a camera array for the image pickup process. (b) The reconstruction process of the Integral imaging setup of (a). (c) Integral imaging setup using a lenslet array and a single imaging sensor. (d) The reconstruction process of the integral imaging setup of (c).

the pickup stage of the synthetic aperture InIm. Figure 1(b) shows the 3D reconstruction of the scene by backpropagation of the captured 2D elemental images through a virtual pinhole. Fig. 1(c) and (d) show the traditional InIm camera pickup and reconstruction process using a single image sensor and a lenslet array. The 2D elemental images can be backpropagated through a virtual pinhole to achieve 3D reconstruction. Reconstructed 3D scene intensity $\mathrm{I}_z(x, y)$ is computed as [44], [45]:

$$\mathrm{I}_z(x,y) = \frac{1}{\mathrm{O}(x,y)} \sum_{m=0}^{M-1} \sum_{n=0}^{N-1} \left[\mathrm{I}_{mn} \left(x - \frac{m \times L_x \times p_x}{z/f}, y - \frac{n \times L_y \times p_y}{z/f} \right) + \epsilon \right] \tag{1}$$

Here (x, y) is the pixel indices, and $\mathrm{O}(x, y)$ is the number of overlapping pixels in (x, y). Additionally, I_{mn} is a 2D elemental image, with (m, n) representing its indices, and (M, N) representing the total number of elemental images. Additionally, (c_x, c_y), (p_x, p_y), and (L_x, L_y) represent the sensor size, the pitch size between cameras, and the resolution of the camera sensor, respectively. z is the reconstruction distance of the 3D object from the InIm system and f is the focal length of the camera lens. ε is the additive camera noise. Assuming the object to be made up of a Lambertian surface with uniform illumination 3D reconstruction at the true depth will minimize the variation of the incoming rays [41].

III. MUTUAL INFORMATION

Recently, spatial mutual information was utilized for integral imaging parameter optimization and integral imaging-based object depth localization [42], [43], and [47]. It uses mutual information to evaluate the fidelity of the 3D integral imaging reconstruction. This can then be used either for passive depth localization of an object present within a 2D bounding box or integral imaging parameter estimation to

optimize some desired quantity like longitudinal resolution. Pixel correspondence-based mutual information ($I(\boldsymbol{X};\boldsymbol{Y})$) between two sub-images $\boldsymbol{X}$ and $\boldsymbol{Y}$ is defined as:

$$I(\boldsymbol{X},\boldsymbol{Y}) = \sum_{g_1 \in \boldsymbol{I_P}} \sum_{g_2 \in \boldsymbol{I}_p} f_{x,y}(g_1, g_2) \log \frac{f_{x,y}(g_1, g_2)}{f_x(g_1) f_y(g_2)} \quad (2)$$

Here $\boldsymbol{I_p}$ is the set of pixel intensity values available in the image, and g_1 and g_2 are pixel intensity values in images $\boldsymbol{X}$ and $\boldsymbol{Y}$ respectively and they take values from the set $\boldsymbol{I}_p$. Additionally, $f_x(g_1)$ and $f_y(g_2)$ represent the probability distribution functions over the pixel intensity values (g_1 and g_2) in $\boldsymbol{X}$ and $\boldsymbol{Y}$ respectively. Additionally, $f_{x,y}(g_1, g_2)$ represents the joint probability distribution function over the pixel intensity values (g_1 and g_2) in $\boldsymbol{X}$ and $\boldsymbol{Y}$. However, this formulation fails to capture the spatial information of an object which can result in poor performance in degraded environments [37]. To remedy this, [43] uses a one-adjacent pixel neighborhood. Some other published methods solve this problem by incorporating gradient information [48] or by using higher-order mutual information [49]. The consequent increase in computational and data requirements can be handled by several methods like principal component analysis or independent component analysis [37]. Volden et al. introduce a graphical approach using the Ising model [50]. It states that the conditional probabilities of a site's gray level corresponding to its neighborhood are proportional to the exponential sum of the potentials of its associated cliques. Thus, different neighborhood configurations that produce the same potential $\mathrm{U}(x)$ can be grouped as a single state α. Mutual information between two images is then given as [50]:

$$I(\boldsymbol{X},\boldsymbol{Y}) = \sum_{g_1 \in \boldsymbol{I_P}} \sum_{g_2 \in \boldsymbol{I_P}} \sum_{\alpha_x} \sum_{\alpha_y} f_{x,y}(g_1, \alpha_x, g_2, \alpha_y) \times \log \frac{f_{x,y}(g_1, \alpha_x, g_2, \alpha_y) f_x(\alpha_x) f_y(\alpha_y)}{f_{x,y}(\alpha_x, \alpha_y) f_x(\alpha_x, g_1) f_y(\alpha_y, g_2)} \quad (3)$$

Here $\boldsymbol{I}_p$ is the set of pixel intensities, and g_1 and g_2 are the intensity values of pixels. Also, α_x and α_y are the unique states corresponding to different neighborhood configurations that produce the same potential. Additionally, f_x and f_y represent the probability distribution functions over the pixel intensity values and energy states in $\boldsymbol{X}$ and $\boldsymbol{Y}$ respectively. Additionally, $f_{x,y}$ represents the joint probability distribution over pixel intensity values and energy states in $\boldsymbol{X}$ and $\boldsymbol{Y}$. Henceforth we use this spatial mutual information formulation to quantify the information contained within an image with respect to a corresponding reference image. We evaluate the efficacy of the 3D InIm method by measuring the mutual information between the 3D reconstructed scene and its ground truth in adverse environmental conditions. We compare this with the mutual information between the 2D central perspective and its ground truth in adverse environmental conditions. In both these computations, the ground truth is assumed to be a 2D clear image without any degradations.

IV. INTEGRAL IMAGING-BASED OBJECT DEPTH LOCALIZATION

We analyze the performance of integral imaging-based object depth localization methods in foggy environments. We experimentally compare three commonly used integral imaging-based object depth localization methods, that is, minimum variance [41], maximum voting [18], and mutual information [42], [43] in foggy environments. In this section, we briefly describe all three object depth localization methods.

A. MINIMUM VARIANCE

The minimum variance (min. var.) [41] method uses a spectral radiance pattern ($\mathrm{L}(\cdot)$) to infer the depth of Lambertian surfaces. It computes the statistical variance of the spectral radiance pattern on each voxel for each camera. The lower the variance, the more likely it is that the information comes from a Lambertian surface point. This is because a Lambertian surface has a uniform radiance pattern. Thus, this method minimizes the variance to estimate the depth. In discrete case the predicted depth is given by [41]:

$$\hat{z}(x,y) = \underset{z \in \boldsymbol{Z}}{\operatorname{argmin}} \sum_{j=1}^{3} \sum_{i=1}^{N} \left[\mathrm{L}(\theta_i, \phi_i, \lambda_j) - I(\lambda_j) \right]^2_{(x,y,z)} \quad (4)$$

Eq. 4 uses N intensity images and three image color bands. Here θ and ϕ are the zenith and azimuthal parameters that determine the ray angle, and λ denotes wavelength. Also, $\mathrm{L}(\cdot)$ is the spectral radiance pattern to capture the radiation intensity at a certain wavelength and direction and $\mathrm{I}(\cdot)$ is the average spectral radiance at a certain wavelength over all directions. The main drawbacks of this strategy are that i) the accuracy of depth localization is sensitive to the types of object surfaces with Lambertian surfaces giving the highest accuracy, and ii) it is especially noisy at the boundary of the surfaces. Assuming bounding box size of $n \times m$ pixels and patch size for computing depth for each pixel as $a \times b$ pixels, the time complexity of this method is $O(l(nm \times ab))$. Here, O is the order of complexity, and l is the number of 3D reconstructions performed to compute the depth.

B. MAXIMUM VOTING

The maximum voting method (max. vote) generates a depth map by using a voting strategy [18]. The voting is performed using local information for each pixel. Thus, compared to the minimum variance method, this method can obtain better results for different types of object surfaces and objects with sharp boundaries. Consider a camera array with each camera denoted as C_k, with $||C||$ being the total number of cameras, and R denoting the central camera. Each camera C_k gives rise to an elemental image E_k. Let $E_k(x, y, C_k)$ denote the intensity of the pixel (x, y) in the elemental image E_k due to camera C_k, and $E(i, j, R)$ denote the intensity of the pixel (i, j) in the central elemental image E due to central camera R. Euclidean distance between the pixel (i, j) from the central

camera R, and pixels (x, y) from each camera C_k is [39]:

$$\mathrm{d}_{i,j}(x,y) = \sqrt{\sum_{k}^{\|C\|} \left(E_k\left(x, y, C^k\right) - E(i,j,R)\right)^2} \quad (5)$$

Now, consider a small window $W_{i,j}$ surrounding the pixel (i, j). Distance $\mathrm{d}_{i,j}$ is computed for the pixel (i, j) at each position inside the window $W_{i,j}$ and accumulated in V as follows [39]:

$$\mathrm{V}(i,j,z) = \frac{\sum_{x,y}^{W_{i,j}} \mathrm{e}^{-\frac{\left(\mathrm{d}_{i,j}(x,y)\right)^2}{\mathrm{THR}}}}{\mathrm{CoK}_{i,j}} \quad (6)$$

Here $\mathrm{CoK}_{i,j}$ is the weight factor to account for only those cameras that see the pixel (i, j), i.e. some positions of the scene in the reference image R are only seen by certain cameras. Depth is now estimated based on the maximum number of votes $\hat{\mathrm{z}}(x, y) = \arg\max \mathrm{V}(i, j, z)$. Assuming bounding box size of $n \times m$ pixels and patch size for computing depth for each pixel as $a \times b$ pixels, the time complexity of this method is $O(l(nm \times ab))$. Here, O is the order of complexity, and l is the number of 3D reconstructions performed to compute the depth.

C. MUTUAL INFORMATION

The mutual information-based object depth localization method [42], [43] uses spatial mutual information (see Eq. 3) to compute the fidelity of the 3D InIm reconstructed scene which can then be used for passive depth localization of an object present within a 2D bounding box. The mutual information is computed between the object's 2D bounding box in the 3D reconstructed scene and the corresponding bounding box in the 2D elemental image. This method generates a mutual information curve as a function of reconstruction depth. The object depth is estimated by locating the curve's maximum. This method performs computation on the entire 2D bounding box of an object as opposed to a patch-based analysis used in both minimum variance and maximum voting methods. It, thus, is more robust to environmental degradation. However, this method is limited to one depth localization per 2D bounding box as opposed to a detailed depth map generated by minimum variance and maximum voting methods. The computation of mutual information curve can be broken down into three parts: InIm 3D reconstruction, mutual information computation, and mutual information curve generation. Assuming bounding box size of $n \times m$ pixels, the combined time complexity of these three steps is $O\left(l\left(nm + b_1^2 b_2^2\right)\right)$ [42], [43]. Here, b_1 and b_2 are the bin sizes for possible pixel values, and possible clique potentials (see section III) and l is the number of 3D reconstructions used to generate the average MI curve. Detailed descriptions of various depth localization approaches discussed in previous sub-sections are provided in references [18], [41], [42], [43] which provide full details on mathematical development of the algorithms and experimental examples.

V. INTEGRAL IMAGING-BASED OBJECT DEPTH LOCALIZATION

A large database of 3D images could be helpful to generalize our results. However, to the best of our knowledge 3D integral imaging databases in degraded environments are not publicly available. As such, we use a laboratory experimental setup to capture a scene in various degraded environments. The laboratory scene contains three objects of interest - a mannequin, a thermal mannequin, and an iron. The scene is captured using 25 (5 vertical $\times$ 5 horizontal) elemental images. The horizontal and vertical camera pitches are both set to 50 *mm*. The focal length of each camera lens used in integral imaging set up is 50 *mm* and the exposure time of each camera is 50 *ms*. The scene is recorded using a visible range sCMOS sensor (Hamamatsu C11440-42U). The image sensor contains 2048 $\times$ 2048 pixels, with 6.5 $\mu m \times 6.5$ μm pixel size. The object scene is placed approximately 6 meters in front of the integral imaging setup. Partial occlusion is created by placing artificial leaves in front of the camera. Low illumination condition is created by reducing the light levels and is quantified by photons per pixel. A foggy environment is created by placing a fog chamber in front of the camera and by using a fog-generating device to fill the chamber. The fog chamber is placed in front of the integral imaging system and is approximately of size $110 \times 70 \times 60$ cm^3. The visibility of the scene is controlled by modifying the fog concentration inside the chamber. We quantify the severity of fog with a scattering coefficient computed using the Koschmieder atmospheric scattering model [51]. Koschmieder atmospheric scattering model is used to describe image formation in hazy environments [51]:

$$I(x,y) = J(x,y)t(x,y) + A(1 - t(x,y)) \quad (7)$$

$$t(x,y) = e^{-\beta d(x,y)} \quad (8)$$

Here, $I(x, y)$ is the observed hazy image with (x, y) representing the traditionally used x and y directions of the rectilinear coordinate systems, $J(x, y)$ is the haze-free image (ideal image), A is the atmospheric light, and $t(x, y)$ is the transmission of the medium that quantifies the fraction of light reaching the sensor. Also, β is the scattering coefficient of the atmosphere that defines the thickness or severity of fog. We use it to quantify our experimental foggy scenes. Here, $d(x, y)$ is the distance between the objects and the imaging sensor. Figure 2(a) shows the scene in a clear environment with all three objects circumscribed by their corresponding 2D bounding boxes. Figure 2(b) shows the same scene in the presence of partial occlusion. Figure 2(c) shows the same scene as Fig. 2(a) in low-illumination of approx. 20 photons per pixel with partial occlusion. Figure 2(d) shows the same scene as Fig. 2(a) with fog (scattering coefficient $\beta = 4.6$) and with partial occlusion. In addition to analyzing the information loss in degraded environments, we also compare three commonly used integral imaging-based object depth localization methods in foggy environments. We capture two laboratory scenes, each in four different fog levels

FIGURE 2. (a) Experimental scene in clear condition. The scene contains three objects of interest with each object being circumscribed by its corresponding 2D bounding box - mannequin is shown in a magenta-colored box, thermal mannequin is shown in a black box, and iron is shown in a red box. (b) The same scene as (a) in the presence of partial occlusion, (c) The same scene as (a) in the presence of low illumination (approximately 20 photons per pixel) and partial occlusion, (d) The same scene as (a) in fog (scattering coefficient $\beta = 4.6$) and partial occlusion.

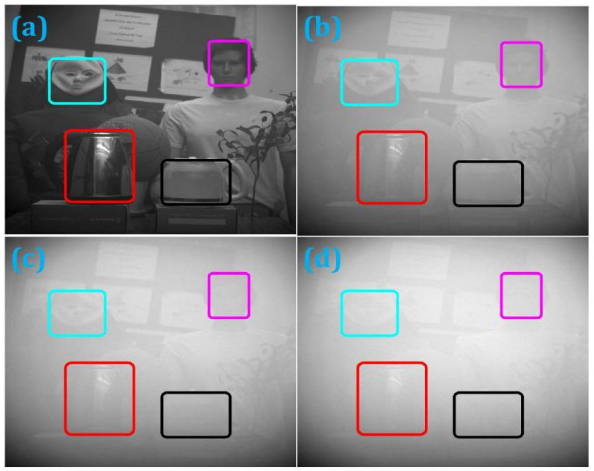

FIGURE 3. First experimental scene in a foggy environment for object depth localization comparison. (a) Scene in mild fog level (scattering coefficient $\beta = 0.5$). Four objects of interest are circumscribed by their corresponding 2D bounding boxes. The four objects are - a mannequin shown in a magenta box, a thermal mannequin shown in a cyan box, a plastic jar shown in a black box, and a metallic jar shown in the red box. (b)–(d) the same scene as (a) with increasing fog severity levels (scattering coefficient $\beta = 3.2, 7.8$, and 9.4 respectively).

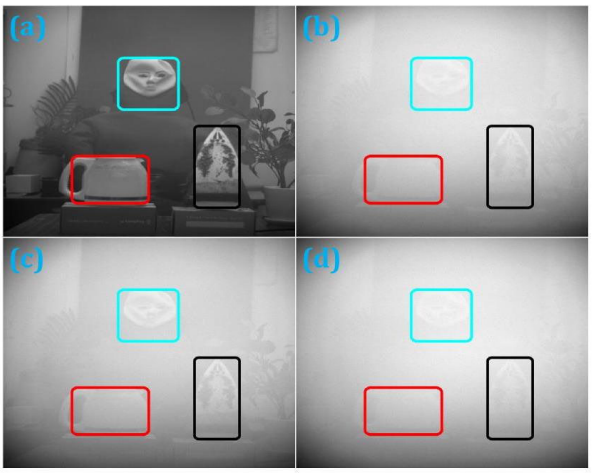

FIGURE 4. Second experimental scene in a foggy environment for object depth localization comparison. (a) Scene in mild fog level (scattering coefficient $\beta = 0.5$). Three objects of interest are circumscribed by their corresponding 2D bounding boxes. The three objects are - a thermal mannequin shown in a cyan box, a plastic jar shown in a red box, and an iron shown in a black box. (b)–(d) the same scene as (a) with increasing fog severity levels (scattering coefficient $\beta = 3.2, 7.8$, and 9.4 respectively).

from mild to severe with scattering coefficient $\beta = 0.5$, 3.2, 7.8, and 9.4 respectively. Figures 3(a)–(d) show the first scene with fog density increasing from (a) to (d) with scattering coefficient $\beta = 0.5$, 3.2, 7.8, and 9.4 respectively. Figures 4(a)–(d) show the second scene with fog density increasing from (a) to (d) with scattering coefficient $\beta = 0.5$, 3.2, 7.8, and 9.4 respectively. The first scene contains four objects of interest - a mannequin, a thermal mannequin, a plastic jar, and a metallic jar. The second scene contains three objects of interest - a thermal mannequin, a plastic jar, and an iron.

VI. RESULTS

A. INFORMATION ANALYSIS IN DEGRADED ENVIRONMENTS

We use the experimental scene shown in Fig. 2 for our analysis. We use spatial mutual information (see Eq. 3) to quantify the information loss in degraded environments. We compute mutual information between an object's 2D bounding box in the target scene and the corresponding bounding box in the reference scene. We use the noiseless scene in an ideal condition (shown in Fig. 2(a)) as the reference scene. Figures 2(a)–(d) are used as target scenes for the 2D case and their corresponding 3D integral imaging reconstructions are used as target scenes for the 3D case. The scenes are 3D reconstructed using integral imaging at each of the object's depths. Figures 5(a)–(c) show 3D reconstructions of the clear scene in Fig. 2(a) at each of the object's depth. Figures 5(d)–(f) show 3D reconstructions of the partially occluded scene in Fig. 2(b) at each of the object's depths. Table 1 shows the average mutual information values for both 2D and 3D cases in clear scene, scene with low light and occlusion, and scene with for and occlusion (see Fig. 2). The average is computed for the three objects (see Fig. 2) - a mannequin, a thermal mannequin, and an iron. Table 1 shows that in clear high illumination environments, only a single 2D image is sufficient to retain most of the information of the scene. For such situations, 3D InIm introduces several imaging artifacts, such as interpolation errors while combining 2D elemental images, that reduce the available information. However, in degraded environments such as partial occlusion, low illumination, fog, or a combination of various degradations. Integral imaging (3D InIm) can

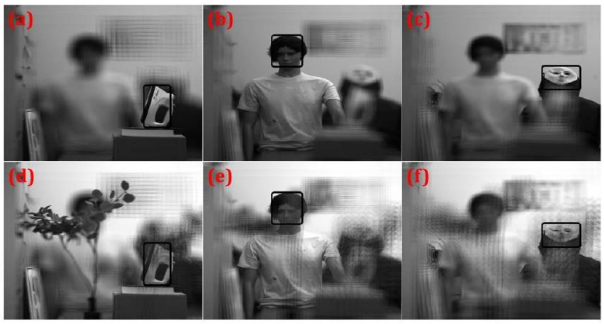

FIGURE 5. (a)–(c) 3D integral imaging reconstruction of the clear scene shown in Fig. 2(a) at each of the object's depths - the iron, the mannequin, and the thermal mannequin respectively. (d)–(f) 3D integral imaging reconstruction of the partially occluded scene shown in Fig. 2(b) at each of the object's depths - the iron, the mannequin, and the thermal mannequin respectively. In each 3D reconstruction, the object in focus is circumscribed with a black colored box.

TABLE 1. 2D vs. 3D average mutual information (MI) comparison for the scene in Fig. 2.

	HI	HI & PO	LI & PO	Fog & PO
2D MI	1.000	0.277	0.173	0.228
3D MI	0.799	0.479	0.411	0.310
% MI	-20%	+73%	+138%	+36%

* HI: High illumination
* PO: Partial occlusion
* LI: Low illumination of approx. 20 photons per pixel.
* Fog: Fog of scattering coefficient $\beta = 4.6$.
* % MI: Percent MI change from 2D to 3D

recover more information about an object than conventional 2D imaging.

B. INFORMATION ANALYSIS IN DEGRADED ENVIRONMENTS

Information loss in degraded environments affects the performance of various imaging applications. As an illustrative example, we experimentally investigate the effect of fog on integral imaging-based object depth localization. We compare three integral imaging-based object depth localization methods - minimum variance (min. var.), maximum voting (max. vote), and mutual information (MI). We use foggy scenes shown in Fig. 3 and Fig. 4. The mutual information-based object depth localization method gives a mutual information curve as a function of reconstruction depth. The object's depth is estimated by searching the location of the mutual information maximum. The other two methods (min. var. and max. vote) generate depth maps. Object depth is estimated by first plotting a pixel depth distribution curve, that is, a histogram of the depths of every pixel present within the object's 2D bounding box, and then locating its maximum. Mutual information curves and pixel depth distribution curves for all the objects in Fig. 3 and Fig. 4 are shown in Appendix. Table 2 compares the accuracy of three integral imaging object depth localization methods. In our experiments, we classify an object's depth localization as correct if it is within 15 *cm* of the true value. We allow this tolerance to counter two sources of error in the measurement of the true depth - first, the objects are not planar but have a 3D profile, and second, true depth measurement techniques (e.g. laser meter) themselves give measurement and alignment errors. A potential source of error in the minimum variance and maximum voting results shown in Table 2 arises from the accumulation of pixel depth values lower than the minimum value considered and higher than the maximum value considered in the first and last buckets of the histogram. This introduces errors as minimum variance and maximum voting methods estimate an object's depth by finding the location of the histogram bucket with the most pixels (or the location of the maximum of the pixel distribution curve). One solution to mitigate this is to remove the first and last buckets from consideration. Table 3 shows the same results as that of Table 2 but with the first and last histogram buckets removed from consideration.

Table 2 and Table 3 show that all three methods (minimum variance, maximum voting, and mutual information) can localize object depth with good accuracy in case of no or very little fog. However, for moderate to severe fog levels, minimum variance and maximum voting algorithms fail to provide a reasonably accurate estimate. Meanwhile, mutual information can provide a reasonably accurate depth estimate because it uses statistics of the entire object contained within the bounding box instead of local patch-based analysis.

TABLE 2. 2D vs. 3D average mutual information (MI) comparison for the scene in Fig. 2.

	MinV	MaxV	MI
Fog1	100%(7/7)	100%(7/7)	100%(7/7)
Fog2	28.57%(2/7)	14.28%(1/7)	100%(7/7)
Fog3	14.28%(1/7)	14.28%(1/7)	100%(7/7)
Fog4	0%(0/7)	0%(0/7)	71.42%(5/7)

* MinV: minimum variance accuracy
* MaxV: maximum voting accuracy
* MI: mutual information accuracy
* Fog1: fog level 1 (Fig. 3(a), Fig. 4(a), $\beta = 0.5$)
* Fog2: fog level 1 (Fig. 3(b), Fig. 4(b), $\beta = 3.2$)
* Fog3: fog level 1 (Fig. 3(c), Fig. 4(c), $\beta = 7.8$)
* Fog4: fog level 1 (Fig. 3(d), Fig. 4(d), $\beta = 9.4$)
* Fractions in brackets (x / 7) represent the number of objects whose depths are accurately localized out of a total of 7 objects considered in scenes shown in Fig. 3 and Fig. 4.

TABLE 3. Modified accuracy of InIm-based object depth localization methods in fog for seven objects shown in Fig. 3 and Fig. 4.

	MinV	MaxV	MI
Fog1	100%(7/7)	100%(7/7)	100%(7/7)
Fog2	28.57%(2/7)	57.14%(4/7)	100%(7/7)
Fog3	14.28%(1/7)	28.57%(2/7)	100%(7/7)
Fog4	0%(0/7)	14.28%(1/7)	71.42%(5/7)

* MinV: minimum variance accuracy
* MaxV: maximum voting accuracy
* MI: mutual information accuracy
* Fog1: fog level 1 (Fig. 3(a), Fig. 4(a), $\beta = 0.5$)
* Fog2: fog level 1 (Fig. 3(b), Fig. 4(b), $\beta = 3.2$)
* Fog3: fog level 1 (Fig. 3(c), Fig. 4(c), $\beta = 7.8$)
* Fog4: fog level 1 (Fig. 3(d), Fig. 4(d), $\beta = 9.4$)
* Fractions in brackets (x / 7) represent the number of objects whose depths are accurately localized out of a total of 7 objects considered in scenes shown in Fig. 3 and Fig. 4.

In these fog levels, the maximum voting algorithm provides better accuracy than the minimum variance method. For dense fog all three methods become unreliable. Still, even in dense fog, the estimates provided by the mutual information algorithm are much more accurate than those provided by the other two methods.

VII. CONCLUSION

In this manuscript, we evaluated the performance of 3D InIm by comparing the mutual information between 1) 3D reconstructed degraded scene and 2D clear non-degraded ground truth, and 2) 2D image of the degraded scene and 2D clear non-degraded ground truth. The degradations considered are fog, partial occlusion, and low light. It is observed that for clear non-degraded environments, the 3D integral imaging introduces artifacts that reduce the amount of available information. However, in degraded environments, such as partial occlusion, low light with partial occlusion, and fog with partial occlusion, 3D integral imaging can recover more information about an object compared to 2D imaging. To demonstrate one of the effects of information loss in degraded environments, we experimentally analyzed the performance of integral imaging-based object depth localization in fogy environments. We compared the performance of three integral imaging-based object depth localization techniques on laboratory scenes in foggy environments. In clear or low fog environments, all three algorithms (minimum variance, maximum voting, and mutual information) perform reasonably well. However, minimum variance and maximum voting algorithms perform more poorly than mutual information in moderate to severe fog levels. For dense fog, all three algorithms fail to provide accurate depth localization of objects. However, even in dense fog, mutual information can provide more accurate estimates compared to minimum variance and maximum voting methods. This manuscript provided preliminary results on experimental scenes. However, a rigorous analysis was not considered here as it is outside of the scope of this manuscript. In the future, more experimental evaluation is needed to get a better understanding of the performance of integral imaging and integral imaging-based object depth localization methods. Additional real-world degradations also need to be tested. One example of such a degradation is brownout conditions which may occur in sandy environments.

Our study shows the potential usefulness of integral imaging in computer vision tasks such as object depth localization under degraded environments. For the degraded scenes we used, experiments illustrate that 3D Integral imaging experiments performs better than 2D imaging in terms of mutual information to preserve object information, which can be beneficial in object detection, depth estimation, or object tracking. Additionally, we analyzed three integral imaging based depth localization methods to show their advantages and limitations in degraded environments. This entire study relies on accurate information about object bounding box. We assume the availability of this bounding box using several deep learning or machine learning methods. However, inaccuracies in obtaining bounding boxes may lead to poor object depth localization performance.

APPENDIX

We plot the mutual information curves and pixel depth distribution curves, this is, a histogram of the depths of every pixel present within the object's 2D bounding box, for all objects in Fig. 3 and Fig. 4 using minimum variance (min. var.) and maximum voting method (max. vote). It can be seen from these figures that minimum variance and maximum voting algorithms perform worse than mutual information in moderate to severe fog levels. For dense fog, all three algorithms fail to provide accurate depth localization of objects.

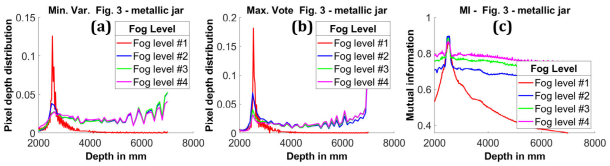

FIGURE 6. (a) Pixel depth distribution, that is, a histogram of the depths of every pixel present within the object's 2D bounding box, of the metallic jar in Fig. 3 using minimum variance (min. var.) method. (b) Pixel depth distribution using maximum voting method (max. vote). (c) Mutual information (MI) curves as a function of reconstruction depth. Four different fog levels are considered here (see Fig. 3(a)–(d)). Fog levels #1–#4 correspond to Fig. 3(a)–(d) respectively with corresponding scattering coefficients β of 0.5, 3.2, 7.8, and 9.4. The true depth of the object is approximately 2540 *mm*.

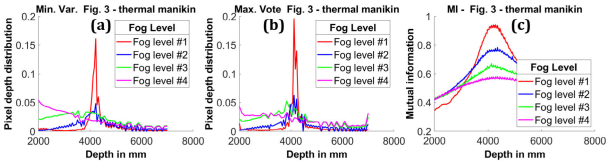

FIGURE 7. (a) Pixel depth distribution, that is, a histogram of the depths of every pixel present within the object's 2D bounding box, of the thermal mannequin in Fig. 3 using minimum variance (min. var.) method. (b) Pixel depth distribution using maximum voting method (max. vote). (c) Mutual information (MI) curves as a function of reconstruction depth. Four different fog levels are considered here (see Fig. 3(a)–(d)). Fog levels #1–#4 correspond to Fig. 3(a)–(d) respectively with corresponding scattering coefficients β of 0.5, 3.2, 7.8, and 9.4). The true depth of the object is approximately 4200 *mm*.

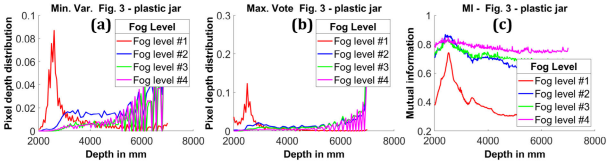

FIGURE 8. (a) Pixel depth distribution, that is, a histogram of the depths of every pixel present within the object's 2D bounding box, of the plastic jar in Fig. 3 using minimum variance (min. var.) method. (b) Pixel depth distribution using maximum voting method (max. vote). (c) Mutual information (MI) curves as a function of reconstruction depth. Four different fog levels are considered here (see Fig. 3(a)–(d)). Fog levels #1–#4 correspond to Fig. 3(a)–(d) respectively with corresponding scattering coefficients β of 0.5, 3.2, 7.8, and 9.4). The true depth of the object is approximately 2500 *mm*.

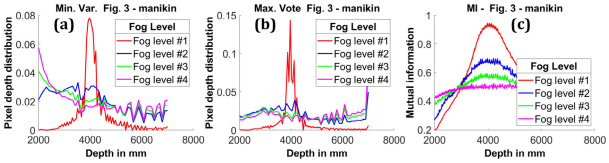

FIGURE 9. (a) Pixel depth distribution, that is, a histogram of the depths of every pixel present within the object's 2D bounding box, of the mannequin in Fig. 3 using minimum variance (min. var.) method. (b) Pixel depth distribution using maximum voting method (max. vote). (c) Mutual information (MI) curves as a function of reconstruction depth. Four different fog levels are considered here (see Fig. 3(a)–(d)). Fog levels #1–#4 correspond to Fig. 3(a)–(d) respectively with corresponding scattering coefficients β of 0.5, 3.2, 7.8, and 9.4). The true depth of the object is approximately 4000 *mm*.

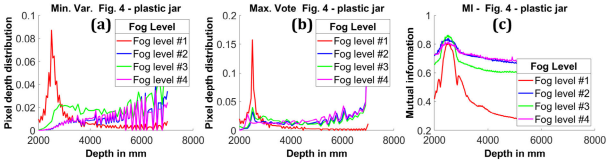

FIGURE 10. Pixel depth distribution, that is, a histogram of the depths of every pixel present within the object's 2D bounding box, of the plastic jar in Fig. 4 using minimum variance (min. var.) method. (b) Pixel depth distribution using maximum voting method (max. vote). (c) Mutual information (MI) curves as a function of reconstruction depth. Four different fog levels are considered here (see Fig. 4(a)–(d)). Fog levels #1–#4 correspond to Fig. 4(a)–(d) respectively with corresponding scattering coefficients β of 0.5, 3.2, 7.8, and 9.4). The true depth of the object is approximately 2500 *mm*.

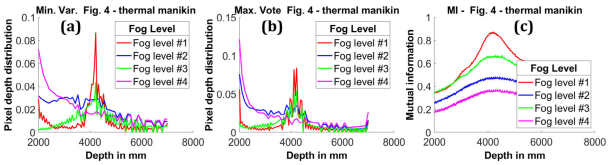

FIGURE 11. (a) Pixel depth distribution, that is, a histogram of the depths of every pixel present within the object's 2D bounding box, of the thermal mannequin in Fig. 4 using minimum variance (min. var.) method. (b) Pixel depth distribution using maximum voting method (max. vote). (c) Mutual information (MI) curves as a function of reconstruction depth. Four different fog levels are considered here (see Fig. 4(a)–(d)). Fog levels #1–#4 correspond to Fig. 4(a)–(d) respectively with corresponding scattering coefficients β of 0.5, 3.2, 7.8, and 9.4). The true depth of the object is approximately 4200 *mm*.

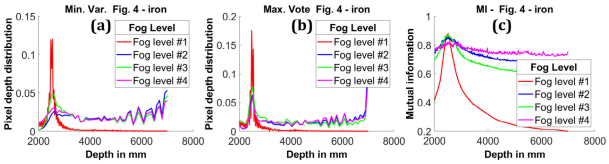

FIGURE 12. (a) Pixel depth distribution, that is, a histogram of the depths of every pixel present within the object's 2D bounding box, of the iron in Fig. 4 using the minimum variance (min. var.) method. (b) Pixel depth distribution using maximum voting method (max. vote). (c) Mutual information (MI) curves as a function of reconstruction depth. Four different fog levels are considered here (see Fig. 4(a)–(d)). Fog levels #1–#4 correspond to Fig. 4(a)–(d) respectively with corresponding scattering coefficients β of 0.5, 3.2, 7.8, and 9.4). The true depth of the object is approximately 2500 *mm*.

REFERENCES

[1] A. S. Komatsu, A. Markman, A. Mahalanobis, K. Chen, and B. Javidi, "Three-dimensional integral imaging and object detection using long-wave infrared imaging," *Appl. Opt.*, vol. 56, no. 9, pp. D120–D126, Mar. 2017.

[2] A. Markman and B. Javidi, "Learning in the dark: 3D integral imaging object recognition in very low illumination conditions using convolutional neural networks," *OSA Continuum*, vol. 1, no. 2, pp. 373–383, Oct. 2018.

[3] D. Aloni, A. Stern, and B. Javidi, "Three-dimensional photon counting integral imaging reconstruction using penalized maximum likelihood expectation maximization," *Opt. Exp.*, vol. 19, no. 20, pp. 19681–19687, Sep. 2011.

[4] X. Shen, A. Carnicer, and B. Javidi, "Three-dimensional polarimetric integral imaging under low illumination conditions," *Opt. Lett.*, vol. 44, no. 13, pp. 3230–3233, Jul. 2019.

[5] B. Tavakoli, B. Javidi, and E. Watson, "Three dimensional visualization by photon counting computational Integral Imaging," *Opt. Exp.*, vol. 16, no. 7, pp. 4426–4436, Mar. 2008.

[6] G. Lippmann, "Epreuves reversibles donnant la sensation du relief," *J. Phys.*, vol. 7, no. 1, pp. 821–825, 1908.

[7] N. Davies, M. McCormick, and L. Yang, "Three-dimensional imaging systems: A new development," *Appl. Opt.*, vol. 27, no. 21, pp. 4520–4528, Nov. 1988.

[8] H. Arimoto and B. Javidi, "Integral three-dimensional imaging with digital reconstruction," *Opt. Lett.*, vol. 26, no. 3, pp. 157–159, Feb. 2001.

[9] F. Okano, H. Hoshino, J. Arai, and I. Yuyama, "Real-time pickup method for a three-dimensional image based on integral photography," *Appl. Opt.*, vol. 36, no. 7, pp. 1598–1603, Mar. 1997.

[10] M. Martinez-Corral, A. Dorado, J. C. Barreiro, G. Saavedra, and B. Javidi, "Recent advances in the capture and display of macroscopic and microscopic 3-D scenes by integral imaging," *Proc. IEEE*, vol. 105, no. 5, pp. 825–836, May 2017.

[11] A. Stern and B. Javidi, "Three-dimensional image sensing and reconstruction with time-division multiplexed computational integral imaging," *Appl. Opt.*, vol. 42, no. 35, pp. 7036–7042, Mar. 2003.

[12] E. H. Adelson and J. R. Bergen, "The plenoptic function and the elements of early vision," *Comput. Models Vis. Process.*, vol. 1, no. 2, pp. 3–20, 1991.

[13] J. Liu, D. Claus, T. Xu, T. Keßner, A. Herkommer, and W. Osten, "Light field endoscopy and its parametric description," *Opt. Lett.*, vol. 42, no. 9, pp. 1804–1807, May 2017.

[14] G. Scrofani, J. Sola-Pikabea, A. Llavador, E. Sanchez-Ortiga, J. C. Barreiro, G. Saavedra, J. Garcia-Sucerquia, and M. Martinez-Corral, "FIMic: Design for ultimate 3D-integral microscopy of in-vivo biological samples," *Biomed. Opt. Exp.*, vol. 9, no. 1, pp. 335–346, Jan. 2018.

[15] J. Arai, E. Nakasu, T. Yamashita, H. Hiura, M. Miura, T. Nakamura, and R. Funatsu, "Progress overview of capturing method for integral 3-D imaging displays," *Proc. IEEE*, vol. 105, no. 5, pp. 837–849, May 2017.

[16] M. Yamaguchi, "Full-parallax holographic light-field 3-D displays and interactive 3-D touch," *Proc. IEEE*, vol. 105, no. 5, pp. 947–959, May 2017.

[17] X. Xiao, B. Javidi, M. M. Corral, and A. Stern, "Advances in three-dimensional integral imaging: Sensing, display, and applications," *Appl. Opt.*, vol. 52, no. 4, pp. 546–560, Jan. 2013.

[18] A. M. Uso, P. L. Carmona, J. M. Sotoca, F. Pla, and B. Javidi, "Depth estimation in integral imaging based on a maximum voting strategy," *J. Display Technol.*, vol. 12, no. 12, pp. 1715–1723, Dec. 2016.

[19] W. A. Roberts and B. S. Thurow, "Correlation-based depth estimation with a plenoptic camera," *AIAA J.*, vol. 55, no. 2, pp. 435–445, Feb. 2017.

[20] Y. Wang, L. Wang, G. Wu, J. Yang, W. An, J. Yu, and Y. Guo, "Disentangling light fields for super-resolution and disparity estimation," 2022, *arXiv:2202.10603*.

[21] L. Shi, C. Liu, D. He, X. Zhao, and J. Qiu, "Matching entropy based disparity estimation from light field data," *Opt. Exp.*, vol. 31, no. 4, pp. 6111–6131, Feb. 2023.

[22] W. Williem and I. K. Park, "Robust light field depth estimation for noisy scene with occlusion," in *Proc. IEEE Conf. Comput. Vis. Pattern Recognit. (CVPR)*, Jun. 2016, pp. 4396–4404.

[23] T.-C. Wang, A. A. Efros, and R. Ramamoorthi, "Depth estimation with occlusion modeling using light-field cameras," *IEEE Trans. Pattern Anal. Mach. Intell.*, vol. 38, no. 11, pp. 2170–2181, Nov. 2016.

[24] H. Sheng, P. Zhao, S. Zhang, J. Zhang, and D. Yang, "Occlusion-aware depth estimation for light field using multi-orientation EPIs," *Pattern Recognit.*, vol. 74, pp. 587–599, Feb. 2018.

[25] X. Jiang, M. L. Pendu, and C. Guillemot, "Depth estimation with occlusion handling from a sparse set of light field views," in *Proc. 25th IEEE Int. Conf. Image Process. (ICIP)*, Oct. 2018, pp. 634–638.

[26] X. Long, L. Liu, C. Theobalt, and W. Wang, "Occlusion-aware depth estimation with adaptive normal constraints," in *Proc. Eur. Conf. Comput. Vis.*, 2020, pp. 640–657.

[27] P. Wani, K. Usmani, G. Krishnan, T. O'Connor, and B. Javidi, "Lowlight object recognition by deep learning with passive three-dimensional integral imaging in visible and long wave infrared wavelengths," *Opt. Exp.*, vol. 30, no. 2, pp. 1205–1218, Jan. 2022.

[28] K. Usmani, T. O'Connor, P. Wani, and B. Javidi, "3D object detection through fog and occlusion: Passive integral imaging vs active (LiDAR) sensing," *Opt. Exp.*, vol. 31, no. 1, pp. 479–491, Jan. 2023.

[29] C. Shannon, "A mathematical theory of communication," *Bell Syst. Tech. J.*, vol. 27, no. 3, pp. 379–423, Jul. 1948.

[30] T. M. Cover and J. A. Thomas, *Elements of Information Theory*, 2nd ed. Hoboken, NJ, USA: Wiley, 1991.

[31] A. Collignon, F. Maes, D. Delaere, D. Vandermeulen, P. Suetens, and G. Marchal, "Automated multi-modality image registration based on information theory," *Inf. Process. Med. Imag.*, vol. 3, no. 6, pp. 263–274, 1995.

[32] P. A. Viola and W. M. Wells III, "Alignment by maximization of mutual information," *Int. J. Comput. Vis.*, vol. 24, no. 2, pp. 137–154, Jun. 1995.

[33] J. West et al., "Comparison and evaluation of retrospective intermodality brain image registration techniques," *J. Comput. Assist. Tomography*, vol. 21, no. 4, pp. 554–568, Jul. 1997.

[34] G. Egnal, "Mutual information as a stereo correspondence measure," UPenn, Philadelphia, PA, USA, Tech. Rep. MS-CIS-00-20, 2000.

[35] F. Maes, A. Collignon, D. Vandermeulen, G. Marchal, and P. Suetens, "Multimodality image registration by maximization of mutual information," *IEEE Trans. Med. Imag.*, vol. 16, no. 2, pp. 187–198, Apr. 1997.

[36] M. Corsini, M. Dellepiane, F. Ponchio, and R. Scopigno, "Image-to-geometry registration: A mutual information method exploiting illumination-related geometric properties," *Comput. Graph. Forum*, vol. 28, no. 7, pp. 1755–1764, 2009.

[37] D. B. Russakoff, C. Tomasi, T. Rohlfing, and C. R. Maurer, "Image similarity using mutual information of regions," in *Proc. Eur. Conf. Comput. Vis. (ECCV)* (Lecture Notes in Computer Science), vol. 3023. Berlin, Germany: Springer, 2004, pp. 596–607.

[38] J. Blazek and B. Zitova, "Image difference visualization based on mutual information," in *Proc. EDS' Contributed Papers*, 2010, pp. 37–41.

[39] C. You, Y. Liu, B. Zhao, and S. Yang, "An objective quality metric for image fusion based on mutual information and muti-scale structural similarity," *J. Softw.*, vol. 9, no. 4, pp. 1050–1054, Apr. 2014.

[40] B. Delabarre and E. Marchand, "Camera localization using mutual information-based multiplane tracking," in *Proc. IEEE/RSJ Int. Conf. Intell. Robots Syst.*, Nov. 2013, pp. 1620–1625.

[41] M. Daneshpanah and B. Javidi, "Profilometry and optical slicing by passive three-dimensional imaging," *Opt. Lett.*, vol. 34, no. 7, pp. 1105–1107, Apr. 2009.

[42] P. Wani, G. Krishnan, T. O. Connor, and B. Javidi, "Information theoretic performance evaluation of 3D integral imaging," *Opt. Exp.*, vol. 30, no. 24, pp. 43157–43171, Nov. 2022.

[43] P. Wani and B. Javidi, "3D integral imaging depth estimation of partially occluded objects using mutual information and Bayesian optimization," *Opt. Exp.*, vol. 31, no. 14, pp. 22863–22884, Jul. 2023.

[44] M. Martínez-Corral and B. Javidi, "Fundamentals of 3D imaging and displays: A tutorial on integral imaging, light-field, and plenoptic systems," *Adv. Opt. Photon.*, vol. 10, no. 3, pp. 512–566, Sep. 2018.

[45] B. Javidi, A. Carnicer, J. Arai, T. Fujii, H. Hua, H. Liao, M. M. Corral, F. Pla, A. Stern, L. Waller, Q. H. Wang, G. Wetzstein, M. Yamaguchi, and H. Yamamoto, "Roadmap on 3D integral imaging: Sensing, processing, and display," *Opt. Exp.*, vol. 28, no. 22, pp. 32266–32293, Oct. 2020.

[46] J. S. Jang and B. Javidi, "Three-dimensional synthetic aperture integral imaging," *Opt. Lett.*, vol. 27, no. 13, pp. 1144–1146, Jul. 2002.

[47] S. R. Narravula, M. M. Hayat, and B. Javidi, "Information theoretic approach for assessing image fidelity in photon-counting arrays," *Opt. Exp.*, vol. 18, no. 3, pp. 2449–2466, Jan. 2010.

[48] J. P. Pluim, J. B. Maintz, and M. A. Viergever, "Image registration by maximization of combined mutual information and gradient information," *IEEE Trans. Med. Imag.*, vol. 19, no. 8, pp. 809–814, Aug. 2000.

[49] D. Rueckert, M. J. Clarkson, D. L. G. Hill, and D. J. Hawkes, "Non-rigid registration using higher-order mutual information," *Proc. SPIE*, vol. 3979, Jun. 2000, Art. no. 804801, doi: 10.1117/12.804801.

[50] E. Volden, G. Giraudon, and M. Berthod, "Information in Markov random fields and image redundancy," in *Proc. 4th Can. Workshop Inf. Theory Appl. II*, 1996, pp. 250–268.

[51] K. He, J. Sun, and X. Tang, "Single image haze removal using dark channel prior," in *Proc. IEEE Conf. Comput. Vis. Pattern Recognit.*, Jun. 2009, pp. 1956–1963.

PRANAV WANI received the B.Tech. degree in mechanical engineering from the Indian Institute of Technology Roorkee, India, and the M.Tech. degree in applied optics from the Indian Institute of Technology Delhi, India. He is currently pursuing the Ph.D. degree with the Electrical and Computer Science Engineering Department, University of Connecticut. His research area is object detection and visualization in low light using 3-D integral imaging and deep learning.

KASHIF USMANI received the B.Sc. degree in physics from the Shibli National College, India, the M.Sc. degree from Aligarh Muslim University, and the M.Tech. degree from the Indian Institute of Technology Delhi, India. He is currently pursuing the Ph.D. degree with the Electrical and Computer Science Engineering Department, University of Connecticut. His research area is object detection and visualization in degraded environments using 3-D polarimetric integral imaging and deep learning.

GOKUL KRISHNAN received the B.Tech. degree in electronics and communication engineering from the Rajagiri College of Engineering, Kochi, and the M.S. degree in electrical engineering from the Indian Institute of Technology Kanpur, India. He is currently pursuing the Ph.D. degree with the Electrical and Computer Engineering Department, University of Connecticut. His research interests include 3-D imaging, gesture recognition, deep learning, and underwater object detection.

BAHRAM JAVIDI (Fellow, IEEE) received the B.S. degree from George Washington University, Washington, DC, USA, and the M.S. and Ph.D. degrees from The Pennsylvania State University, University Park, PA, USA, all in electrical engineering. He is the Board of Trustees Distinguished Professor with the University of Connecticut (UConn), the highest rank and honor bestowed on faculty by UConn, based on research, teaching, and service. He has made seminal contributions to passive and active multi-dimensional imaging from nano to micro and macro scales. His research interests include a broad range of transformative imaging approaches using optics and photonics. His current research activities include digital holography, polarimetric 3-D imaging at low light, 3-D visualization and recognition of objects in photon-starved environments; automated disease identification using biophotonics with compact digital holographic sensors for use in developing countries; optical information security, encryption, and authentication; non-planar flexible 3-D image sensing and bio-inspired imaging.